



# Linear Collider Collaboration Tech Notes

---

## Comparison of Lattice Options for the NLC Main Linac

November 11, 1999

Y. Nosochkov & T. O. Raubenheimer  
Stanford Linear Accelerator Center  
Stanford, California

### *Abstract:*

The goal of this study was to select an optimal lattice for the NLC main linac, based on the analysis and comparison of several lattice options. In this study, we examined the FODO and doublet optics, combinations of 2 vs. 3 accelerator structures per girder, three options for the phase advance per cell and various configurations for the BNS autophasing energy spread. In the lattice analysis, we compared the calculations of emittance growth and misalignment tolerances due to ground motion, as well as magnet parameters

# Comparison of Lattice Options for the NLC Main Linac

Yuri Nosochkov and Tor Raubenheimer  
Stanford Linear Accelerator Center, Stanford University, Stanford, CA 94309

## Abstract

The goal of this study was to select an optimum lattice for the NLC main linac, based on analysis and comparison of several lattice options. In the study we examined the FODO and doublet optics, combinations of 2 vs. 3 accelerator structures per girder, dependence on phase advance per cell, and various profiles of the beam energy spread. In the lattice analysis we compared magnet parameters for different options, results of emittance growth calculations, and machine tolerances due to ground motion.

## 1 Introduction

The NLC main linac is designed to accelerate the beam from 10 GeV up to 500 GeV. The two main components of the linac are the rf-accelerator structures, which occupy most of the linac length, and the quadrupoles. For a loaded accelerating gradient of 55 MeV/m, the combined length of the linac structures is about 9 km. The quadrupoles provide transverse beam focusing while the beam is accelerating.

The ZDR linac design [1] is based on a periodic FODO lattice with accelerator structures placed between the quadrupoles. In this design every two structures are paired together on one girder, and the length of a FODO cell is adjusted for an integral number of girders between the quadrupoles. To provide conditions for the BNS autophasing wakefield compensation with approximately constant energy spread, the linac cell length was gradually increased with the beam energy as  $\sim \sqrt{E}$ . This was done in a step-wise way by dividing the linac into five sections and increasing the number of girders between quads by one girder in each consecutive section. Thus, the cells in sections 1,2,3,4,5 contain 2,4,6,8,10 rf-structures per half-cell, respectively.

The ZDR main linac assumed a SLED-II rf-pulse compression scheme where four structures were powered from the same source. In the ZDR it made sense to separate the structures into rf-girders each holding two structures. The present rf-pulse compressor powers sets of three structures. Thus, at present it would be easier to construct the linac with three structures per girder.

In this study we compare the ZDR-like linac lattice with other lattice options based on rf-girders holding three accelerator structures. Our goal was to select a practical linac lattice which has minimal emittance dilution effects and relaxed machine tolerances. The results of the study are discussed in the following sections.

## 2 Basic Lattice Options

Our primary linac model is based upon a periodic array of FODO cells with accelerator structures placed between the quadrupoles. High periodicity of  $\beta$ -functions reduces effects of chromatic and systematic machine errors on emittance growth. The use of identical cells also simplifies the engineering design.

The focusing in a symmetric FODO cell can be expressed as a function of two parameters: cell length and cell phase advance. In this section we compare two lattice options based on a different

cell length. In particular, these options have different number of rf-structures per half-cell. In addition, we investigate the use of a doublet cell (FDOFDO) in the beginning of the linac.

For a cost effective design we assume that two or more identical accelerator structures are arranged on one girder and the gaps between quadrupoles are compactly filled with an integral number of girders. Accordingly, the cell length can only be varied in steps approximately equal to  $2n_s l_s$ , where  $n_s$  is the number of structures per girder and  $l_s \approx 1.8$  m the length of one structure. With the loaded accelerator gradient of  $\approx 55$  MeV/m, the beam acceleration from 10 to 500 GeV requires about 4950 rf-structures.

## 2.1 Two vs. Three Structures per Girder

In the cell length study we simulated two types of lattice: 1) based on two rf-structures per girder (FODO-2), which is similar to the ZDR design, and 2) based on three structures per girder (FODO-3). For the BNS autophasing wakefield compensation [2] at approximately constant beam energy spread, the linac focusing as a function of beam energy has to be gradually reduced by lengthening the cells and/or reducing the cell phase advance. Similar to the ZDR design, we divided the FODO-2 and FODO-3 lattices into several sections with the number of rf-structures per half-cell increased from section to section approximately as  $\sim \sqrt{E}$  as shown in Fig. 1. For simplicity, we used a constant  $90^\circ$  phase advance per a FODO cell. With the above conditions a comparable quadrupole gradient along the linac can be achieved if the quadrupole length is scaled with energy as  $\sim \sqrt{E}$ .

The transitions between sections were matched by optimizing the last 6 quadrupoles in each section. In addition to matching the transition  $\beta$  and  $\alpha$ -functions, we also minimized the chromatic  $W$ -functions [3]. The latter reduced chromatic perturbation and energy dependent emittance growth caused by break in periodic  $\beta$ -functions between sections. The above optics optimization was done using MAD code [3]. The  $\beta$ -functions for the two lattices are shown in Fig. 2 and 3. Some lattice parameters are listed in Table 1.

## 2.2 Doublet vs. FODO Cells

In addition to the FODO lattice we investigated the use of doublet cells in the beginning of linac. To make a doublet cell we replaced single F and D quadrupoles by FD-doublets to form FDOFDO cells. For the same phase advance, the FDOFDO focusing provides smaller and more uniform  $\beta$ -functions compared to the FODO cells. The doublet optics could be advantageous in the beginning of the linac because the wakefield compensation requires stronger focusing at low beam energy.

An example of  $\beta$ -functions in the FODO and doublet cells is shown in Fig. 4 and 5. In both figures the cell length fits 6 rf-structures and the phase advance is  $90^\circ$ . For the above cells, the maximum and minimum  $\beta$ -functions versus cell phase advance are shown in Fig. 6. At large values of the phase advance the FDOFDO cells have much smaller  $\beta$ -functions compared to the FODO lattice. Note that the FDOFDO cell has two periods and, therefore, the resonance increase of  $\beta$ -functions in this cell is expected near the phase advance of  $360^\circ$ .

The disadvantage of the FDOFDO optics is that it doubles the number of quadrupoles and significantly increases the quadrupole strength due to cancellation of some focusing in the doublets. Fig. 7 shows F and D quadrupole strength  $kl$  as a function of cell phase advance for the FODO and FDOFDO cells as described in the previous paragraph, with  $k = \frac{B'}{B\rho}$  and  $l$  being the quad length. It is interesting to note that despite the stronger quadrupoles, the FDOFDO cells generate less linear chromaticity compared to FODO cells. The phase dependence of the cell chromaticity is shown in Fig. 8, where the linear chromaticity is defined as  $\frac{1}{4\pi} \int k\beta ds$  and was calculated with MAD

Table 1: Lattice parameters for the four linac lattice options.

Lattice	FODO-2	FODO-3	FODO-3D6	FODO-3D8
Total length [m]	9715.78	9756.95	9780.27	9780.27
Total number of quads	740	690	748	748
Combined quad length [m]	378.90	430.92	445.55	445.55
Combined quad field $\sum B'l$ [MG]	451.88	443.76	472.15	472.06
Max. quad gradient [kG/m]	1746.1	1686.5	1865.6	1911.1
Total betatron $x/y$ phase [ $2\pi$ ]	92.26/92.26	86.17/86.18	85.32/85.27	85.35/85.26
Number of sections	5	3	4	4
Per section:				
Beam energy at transitions [GeV]	30/80/165/290	45/155	28/45/155	28/45/155
Structures per half-cell	2/4/6/8/10	3/6/9	3/3/6/9	3/3/6/9
Cell phase advance [ $^\circ$ ]	90	90	80/90/90/90	80/90/90/90
Quad length [cm]	20/30/40/60/80	25/50/80	25/25/50/80	25/25/50/80

for  $90^\circ$  cells containing 6 rf-structures. The significant cancellation of the FDOFDO quadrupole chromaticity is due to near-equal  $\beta$ -functions in the F and D doublet quadrupoles. It should be noted that the desired energy spread for BNS damping is roughly inversely proportional to the chromaticity, and thus the lower doublet chromaticity has no advantage for wakefield compensation.

To investigate the effect of strong doublet focusing at low beam energy, we simulated the third lattice (FODO-3D6) which is the same as the FODO-3 lattice except the  $90^\circ$  FODO cells in the first half of the first section are replaced by  $80^\circ$  FDOFDO cells. The  $\beta$ -functions for the FODO-3D6 lattice are shown in Fig. 9. As in the FODO-3 lattice, the doublet cells have 3 rf-structures per half-cell.

The transition matching between the doublet and FODO sections was done with 6 variable quadrupoles. As seen in Fig. 9, the 6-quad match results in rather large transition  $\beta$ -functions which might enhance linac chromaticity. This  $\beta$  and chromatic perturbation can be reduced if 8 matching quadrupoles are used. To study the transition chromaticity we made FODO-3D8 doublet lattice, shown in Fig. 10, which is the same as the FODO-3D6 lattice, but with 8 transition quadrupoles. The lattice parameters for these two options are given in Table 1.

### 2.3 Lattice Comparison

In terms of magnet parameters listed in Table 1, the FODO lattice has an advantage with respect to the doublet+FODO lattice because of less number of quadrupoles and a shorter linac. Among the four options the FODO-3 lattice requires the minimal combined quadrupole field  $\sum B'l$ .

In the next sections we will compare the four lattices in terms of chromatic emittance growth and ground motion tolerances. To simplify calculations below, the small focusing effects in the accelerator structures were neglected.

### 2.3.1 Momentum Bandwidth

The deviation of the particle energy from the nominal value due to energy spread in the bunch and field errors in the structures leads to variation in quadrupole focusing and energy dependent amplitude of betatron oscillations. In the first order, each quadrupole generates chromatic betatron perturbation  $\Delta\beta$  which propagates along the linac as

$$\frac{\Delta\beta_i}{\beta}(s) = \delta(kl\beta)_i \sin 2[\mu(s) - \mu_i], \quad (1)$$

where  $i$  is the quadrupole index and  $\delta = \frac{\Delta p}{p}$ . The total change in  $\beta$  with energy is obtained by summation of individual quadrupole contributions.

In a periodic lattice the chromatic  $\beta$ -perturbations from quadrupoles with the same strength and  $\beta$ -functions tend to compensate each other over several cells due to uniform quadrupole distribution in betatron phase. The perturbations in the non-periodic regions, such as transition sections in the linac lattice, may propagate uncompensated and lead to emittance growth through filamentation in the phase space. The chromatic emittance growth can be expressed in terms of  $B_{mag}$  function [4, 5]:

$$\frac{\Delta\epsilon}{\epsilon} = \langle B_{mag} \rangle_\delta - 1, \quad (2)$$

$$B_{mag}(\delta) = \frac{1}{2} \left\{ \frac{\beta(\delta)}{\beta(0)} + \frac{\beta(0)}{\beta(\delta)} + \left[ \alpha(\delta) \sqrt{\frac{\beta(0)}{\beta(\delta)}} - \alpha(0) \sqrt{\frac{\beta(\delta)}{\beta(0)}} \right]^2 \right\}, \quad (3)$$

where  $\alpha(0)$  and  $\beta(0)$  are on-momentum lattice functions ( $\delta = 0$ ).

The  $B_{mag} - 1$  function along the linac for a constant  $\delta = \pm 2\%$  is shown in Fig. 11–14 for the above four lattice options. Note that the FODO-2 and FODO-3 options have comparable amplitude of the  $B_{mag} - 1$ . In the FODO-3D6 case the initial amplitude in the doublet section is very small, but after the transition it gets a factor of 2 larger than in the FODO-2 and 3 lattice. The reason for the increased chromaticity is the large  $\beta$ -perturbation in the 6-quad transition between the doublet and FODO sections (see Fig. 9). This local  $\beta$ -perturbation acts as a single source of chromaticity which then propagates uncompensated along the linac. The less smoother match in this transition is due to larger difference between doublet and FODO  $\beta$ -functions compared to transitions between FODO cells. By using 8 matching quadrupoles in this transition in the FODO-3D8 lattice, the  $\beta$ -perturbation and the  $B_{mag} - 1$  function were reduced to the same level as in the FODO-2 and 3 lattice.

The momentum dependence of the  $B_{mag} - 1$  function at the end of each lattice is shown in Fig. 15–18. These curves characterize emittance growth as a function of  $\delta$  and can be considered as a momentum bandwidth of the linac lattice. The plots show that there is no significant difference in momentum bandwidth among the studied lattices, provided that the transition chromaticity is minimized.

### 2.3.2 Tolerances

Another comparison of the linac options included calculation of tolerances for quadrupole and structure rms misalignment and quadrupole jitter due to ground motion. The results are shown in Table 2, where the tolerances for quad and structure misalignment correspond to 6% emittance growth, and tolerance for quadrupole jitter corresponds to induced orbit jitter with amplitude equal

Table 2: Misalignment and jitter tolerances for the four linac lattice options.

Lattice		FODO-2	FODO-3	FODO-3D6	FODO-3D8
Quad rms motion for 6% emittance dilution [ $\mu\text{m}$ ]	$x$	50.1	64.8	31.9	32.0
	$y$	5.0	6.5	3.1	3.1
RF-structure rms motion for 6% emittance dilution [ $\mu\text{m}$ ]	$x$	20.4	19.5	19.6	19.6
	$y$	2.04	1.95	1.96	1.96
Quad jitter for 25% beam size orbit jitter [nm]	$x$	70.6	71.2	67.2	67.2
	$y$	7.1	7.1	6.7	6.7

to 25% of beam size. The calculations were done for  $N = 1.1 \cdot 10^{10}$  particles per bunch,  $\sigma_z = 150 \mu\text{m}$  of the bunch length,  $W'_\perp = 1.08 \cdot 10^{20} \text{ V/C/m}^3$  of transverse wakefield slope in the structures, and  $\gamma\epsilon_x = 3 \cdot 10^{-6} \text{ m}$  and  $\gamma\epsilon_y = 3 \cdot 10^{-8} \text{ m}$  of beam normalized emittance. Note that the above value of  $W'_\perp$  corresponds to rf-structures with  $a/\lambda = 0.17$ , while in the present NLC design the structures have  $a/\lambda = 0.18$  with short range transverse wakefield lower by about 20%. Here,  $a$  is the iris radius in the structures, and  $\lambda$  is the wavelength of the fundamental accelerating field mode. In the approximation used in the tolerance calculations [6], the accelerator structures were treated as if they occupied all the space between the quadrupoles without any gaps.

Table 2 shows that the FODO options have an advantage with respect to the doublet+FODO lattice in terms of quadrupole misalignment and jitter tolerances. This is likely due to larger dispersive effects in the strong doublet cells. For a similar reason the FODO-3 lattice has 30% better quadrupole misalignment tolerances compared to the FODO-2 lattice. The structure misalignment tolerances are determined by the wakefield value and are about the same for the four options. This arises because the average  $\beta$ -functions are not significantly different in the above lattice options (see Fig. 2,3,9 and 10).

Based on this comparison of magnet parameters, calculations of chromatic emittance growth and tolerances for quadrupole misalignment and jitter, we conclude that the FODO-3 lattice has an advantage with respect to the other options. It requires less number of quadrupoles, less combined quadrupole field and has better misalignment tolerances.

### 3 Phase Advance Options

Following the conclusion of the previous section we limited the further study to the FODO-3 type lattice. In this section, we discuss the ground motion tolerances and emittance growth in the linac as a function of phase advance per cell.

#### 3.1 Lattice

As mentioned earlier, the BNS autophasing wakefield compensation with constant  $\sigma_p/p$  can be achieved by reducing the cell focusing with the beam energy. This is done by gradually increasing the cell length and/or reducing the phase advance per cell. As described in the previous sections, the FODO-3 lattice provides a step-wise increase of the cell length from section to section proportionally to  $\sqrt{E}$ . In a FODO lattice, the desired BNS energy spread can be estimated as:

$$\left(\frac{\sigma_p}{p}\right)_{BNS} \approx \frac{Nr_0W'_\perp\sigma_z L_c^2}{4\gamma} \frac{L_c^2}{6} \left(1 + \frac{3}{2}ctn^2\frac{\mu_c}{2}\right), \quad (4)$$

where  $N$ ,  $r_0$ ,  $L_c$ ,  $\mu_c$  and  $\gamma$  are, respectively, the number of particles per bunch, the classical electron radius, the cell length, phase advance per cell, and the Lorentz factor. This energy spread is inversely dependent on the beam energy and, over the region of interest, roughly inversely proportional to the chromaticity. Thus, to achieve a better match between the beam and desired BNS autophasing energy spread within each section, the FODO-3 lattice was modified to provide reduction of the cell phase advance  $\mu_c$  with the beam energy  $E$ ,

$$\mu_c = \mu_{c0} \left(\frac{E}{E_0}\right)^a, \quad (5)$$

where index '0' refers to the beginning of each section and  $a = [-0.3, -0.3, 0]$  in the 1st, 2nd and 3rd linac sections, respectively. In addition, a  $5^\circ$  split was introduced between the  $y$  and  $x$  cell phase advance to reduce the effects of betatron coupling due to machine errors, ion, and space charge effects. All the lattice modifications were done using a special linac matching code [7] which automatically generates the complete matched FODO lattice with desired parameters and phase advance variation.

To study dependence on the cell phase advance we generated three linac options named FODO-100, FODO-120 and FODO-140 with the lattice parameters listed in Table 3. The  $\beta$ -functions in the FODO-100 and FODO-120 lattices are shown in Fig. 19, 20 and the profile of the phase advance per cell for the FODO-100 lattice is shown in Fig. 21.

Due to phase advance variation with the beam energy (Eq. 5), the FODO optics in the first two linac sections is no longer exactly periodic. However, it still provides sufficient compensation of chromatic  $\beta$ -perturbations since the change in phase and  $\beta$ -periodicity over a few cells is rather small. In the 3rd linac section the wakefield effects are reduced due to high beam energy. This allows to use smaller phase advance per cell compared to sections 1 and 2. In addition, at the end of linac, the correlated energy spread, used for BNS damping, must be removed because of the limited final focus bandwidth. For this reason, the phase advance per cell in the 3rd section is kept constant, reducing the desired energy spread as the beam is accelerated. In the transitions between linac sections the optics is optimized, but the periodicity of the  $\beta$ -functions and phase advance is not maintained.

Table 3: Lattice parameters for the linac options with different phase advance per cell.

Section	Structures per half-cell	Length [km]	Energy [GeV]	$a$	Initial cell phase advance [°]		
					FODO-100	FODO-120	FODO-140
1	3	0 – 0.7	10 – 45	-0.3	100 / 105	120 / 125	140 / 145
2	6	0.7 – 2.9	45 – 150	-0.3	100 / 105	120 / 125	140 / 145
3	9	2.9 – 10.1	150 – 500	0	85 / 90	100 / 105	120 / 125
Maximum gradient [kG/m]					1634.5	1839.7	2061.9
Total $x/y$ phase [ $2\pi$ ]					78.8 / 83.3	93.4 / 98.1	110.8 / 115.5

### 3.2 Tolerances

In addition to optics matching, the linac code [7] also calculates the ground motion and jitter tolerances, as well as the desired BNS energy spread. The results for the ground motion tolerances are shown in Table 4 for the same beam parameters as in Table 2. In our view, the weaker FODO-100 lattice has an advantage with respect to the other two options. Compared to the  $120^\circ$  lattice, it has 15% better quadrupole misalignment and jitter tolerances, but only 2% tighter the rf-structure tolerance. Comparison of the Tables 2 and 4 indicates that the average focusing in the FODO-100 lattice is slightly weaker than in the FODO-3 lattice with constant  $90^\circ$  phase advance per cell.

### 3.3 BNS Configurations

The desired BNS autophasing energy spread calculated with the linac matching code is shown in Fig. 22, 23 for the FODO-100 and FODO-120 lattices. Note that the stronger  $120^\circ$  optics requires less beam energy spread for autophasing wakefield compensation.

Similar to the ZDR design, we studied 8 configurations for the rf-phase in the linac accelerator structures to generate the beam energy spread. The rf-phase and beam energy at the rf-phase switching points for the 8 BNS configurations are listed in Table 5, and the corresponding beam energy spread is shown in Fig. 24. The 8 BNS configurations provide various level of the nearly constant beam energy spread in most of the linac and decrease the desired  $\sigma_p/p$  to 0.3–0.5% at the end of the linac.

### 3.4 Vertical Emittance Growth

In this section we discuss the results of particle tracking simulations using LIAR code [8], and compare vertical emittance growth in the linac for 8 BNS configurations. In all the simulations the initial conditions of the beam include: a small energy spread  $\sigma_p/p = 10^{-5}$ ; vertical beam offset at the entrance to the linac  $y = 2.2 \mu\text{m}$  ( $\approx 1\sigma_y$ ); normalized emittance of  $\gamma\epsilon_x = 3.6 \cdot 10^{-6}$  and  $\gamma\epsilon_y = 4 \cdot 10^{-8}$ ; and rms bunch length of  $150 \mu\text{m}$  with  $1.1 \cdot 10^{10}$  particles per bunch.

The results of emittance growth at these conditions for 8 BNS configurations are shown in Fig. 25 (a,b,c) for the  $100^\circ$ ,  $120^\circ$  and  $140^\circ$  lattices. One can see that in the FODO-100 lattice the minimum emittance growth is achieved at a higher BNS configuration number compared to the other two options. This is because the weaker lattice requires larger beam energy spread for BNS wakefield compensation. A comparable minimum emittance growth is achieved in the FODO-

Table 4: Misalignment and jitter tolerances for the linac options with different phase advance per cell.

Lattice		FODO-100	FODO-120	FODO-140
Quad rms motion for 6%	$x$	69.1	59.7	50.0
emittance dilution [ $\mu\text{m}$ ]	$y$	6.9	5.9	4.9
RF-structure rms motion for 6%	$x$	18.7	19.1	18.5
emittance dilution [ $\mu\text{m}$ ]	$y$	1.9	1.9	1.8
Quad jitter for 25%	$x$	73.6	64.8	54.5
beam size orbit jitter [nm]	$y$	7.3	6.4	5.3

Table 5: RF-phase in the linac ( $\phi_1, \phi_2, \phi_3$ ) and beam energy at the rf-phase switching points ( $E_1, E_2$ ) for 8 BNS configurations.

Config.	$\phi_1$ [°]	$E_1$ [GeV]	$\phi_2$ [°]	$E_2$ [GeV]	$\phi_3$ [°]
1	4	30	-7	485	-30
2	8	30	-5	455	-30
3	10	30	-3	425	-30
4	12	30	-1	400	-30
5	14	30	1	380	-30
6	16	30	3	360	-30
7	18	30	5	335	-30
8	10	30	7	320	-30

100 and FODO-120 options, but it is larger in the case of FODO-140 lattice. It is likely due to enhancement of the orbit and dispersive effects in the strong  $140^\circ$  optics. Based on this comparison we limited further study to the  $100^\circ$  and  $120^\circ$  options.

Fig. 25 (d) shows the energy overhead parameter which determines the percentage of additional rf-power needed to generate the BNS energy spread. One can see in Fig. 25 that for a minimum emittance growth the stronger optics requires less rf-power in the accelerator structures.

With the same initial beam conditions as above, we also studied the effect of a single quadrupole offset on the emittance growth. The simulations were done for three cases with  $y = 0.5 \mu\text{m}$  vertical offset of a single D-quadrupole at the distance of: 1)  $s = 1.7 \text{ km}$ , 2)  $s = 4.7 \text{ km}$ , and 3)  $s = 8.4 \text{ km}$  from the beginning of the linac. The results for the FODO-100 and FODO-120 lattices as a function of BNS configuration are shown in Fig. 26. Comparison shows that the FODO-100 lattice at BNS configurations 6-8 has the smallest emittance dilution. An example of vertical emittance growth along the linac with offset quadrupoles for the FODO-100 lattice and BNS configuration 7 is shown in Fig. 27. It can be seen that the emittance growth generated in the beginning of linac is significantly damped with the BNS compensation, but the compensation is not sufficient for perturbations generated at the end of linac. Based on the above comparison we selected the FODO-100 option for the linac lattice.

In the last simulation in this study we used LIAR to calculate emittance growth caused by randomly misaligned accelerator structures. For the rms vertical misalignment of  $y_{rms} = 10 \mu\text{m}$ , 20 random seeds of structure offsets were generated and the beam was tracked for 8 BNS configurations. The results of emittance growth are shown in Fig. 28. In agreement with the other simulations for the FODO-100 lattice, the best compensation of the emittance growth due to structure misalignment is obtained with the larger beam energy spread.

## 4 Conclusion

To select the optimum lattice for the NLC main linac, we generated and compared several lattice options based on the FODO and doublet cells, 2 and 3 rf-structures per girder, three choices for the cell phase advance and 8 BNS configurations for the beam energy spread. In the study, we compared the linac options in terms of magnet parameters, magnet alignment and jitter tolerances, emittance growth due to energy errors, beam oscillation and magnet misalignment. As a result, we

selected the FODO-100 type lattice for the main linac optics, which is based on FODO cells with three rf-structures per girder and  $100^\circ$  initial phase advance per cell. Among the studied options, this lattice has the most relaxed tolerances for a quadrupole ground motion, minimum emittance growth and requires less combined quadrupole strength. The details of the present NLC main linac design based on this option can be found in Ref. [7].

## References

- [1] NLC ZDR Design Group, “Zeroth-Order Design Report for the Next Linear Collider,” SLAC Report 474 (1996); with updated parameters at:  
<http://www-project.slac.stanford.edu/lc/nlc-tech.html>.
- [2] V. Balakin *et al.*, “VLEPP: Transverse Beam Dynamics,” Proceedings of the 12th Int. Conf. on High Energy Accelerators, FNAL, 119 (1983).
- [3] H. Grote, F. C. Iselin, CERN/SL/90-13 (AP) Rev.5 (1996).
- [4] F.-J. Decker *et al.*, “Dispersion and Betatron Matching into the Linac,” SLAC-PUB-5484 (1991).
- [5] N. Merminga *et al.*, “Transverse Phase Space in the Presence of Dispersion,” SLAC-PUB-5514 (1991).
- [6] T.O. Raubenheimer, TOLERANCE code (unpublished).
- [7] Y. Nosochkov *et al.*, “Matching Program for the NLC Main Linac,” SLAC note LCC-0023 (1999); on the web at:  
[http://www-project.slac.stanford.edu/lc/ilc/TechNotes/LCCNotes/lcc\\_notes\\_index.htm](http://www-project.slac.stanford.edu/lc/ilc/TechNotes/LCCNotes/lcc_notes_index.htm).
- [8] R. Assmann *et al.*, “LIAR - A Computer Program for the Modeling and Simulation of High Performance Linacs,” SLAC/AP-103 (1997).

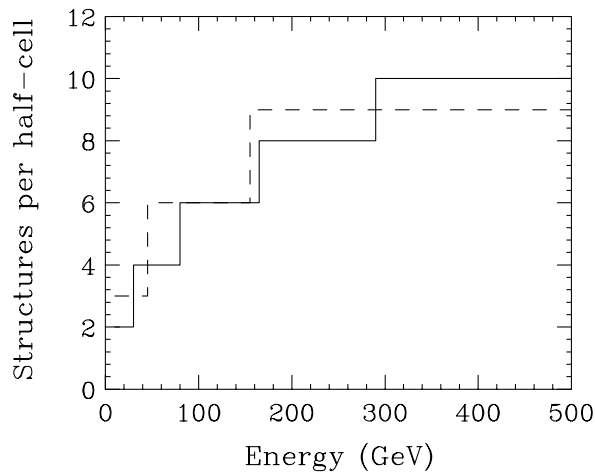


Figure 1: Number of accelerator structures per half-cell vs. beam energy for FODO-2 (solid) and FODO-3 (dash) lattices.

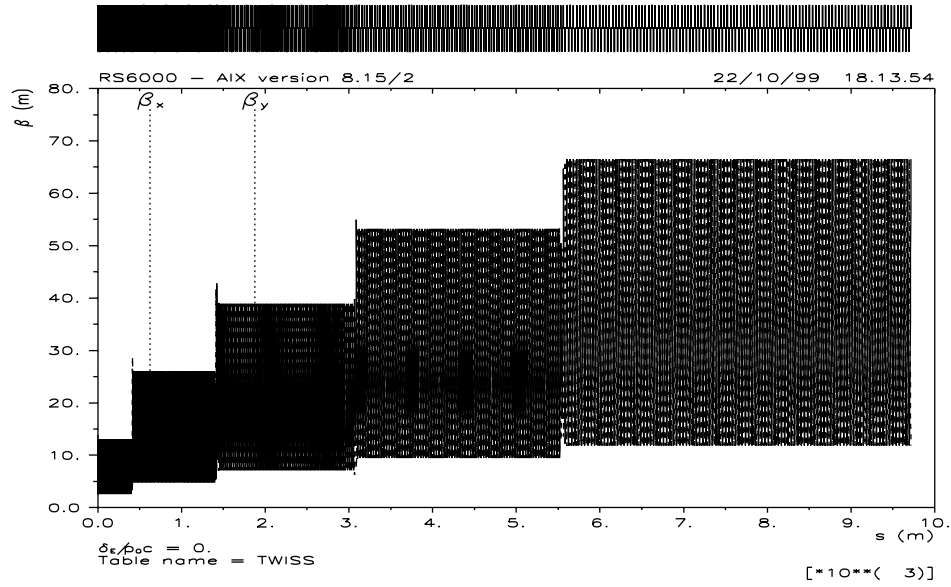


Figure 2:  $\beta$ -functions in the  $90^\circ$  FODO-2 lattice based on 2 rf-structures per girder.

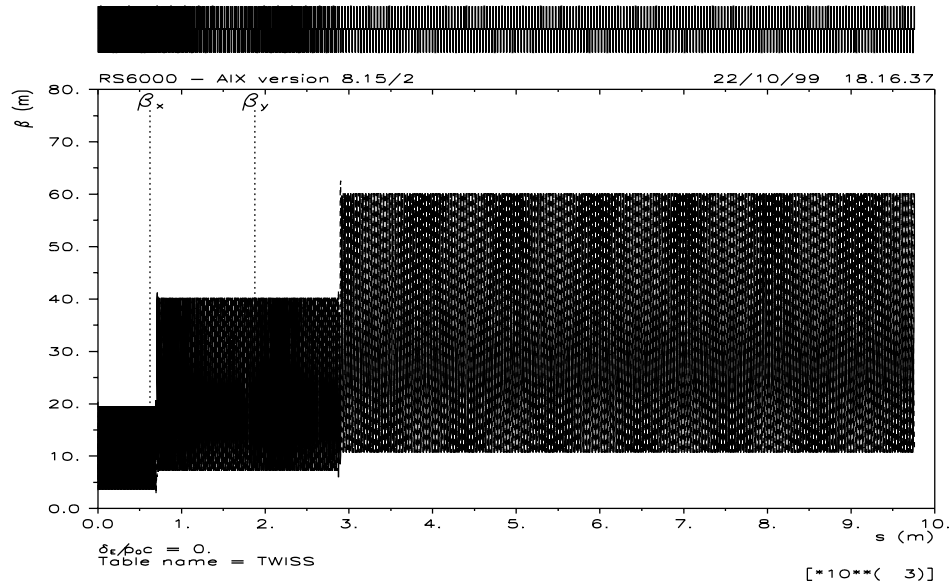


Figure 3:  $\beta$ -functions in the  $90^\circ$  FODO-3 lattice based on 3 rf-structures per girder.

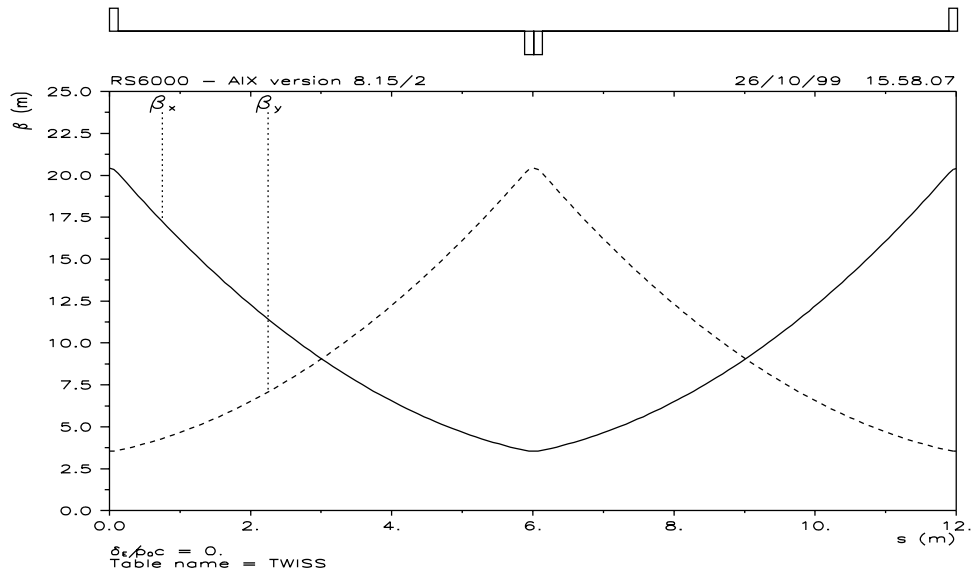


Figure 4:  $\beta$ -functions in the  $90^\circ$  FODO cell with 3 rf-structures per half-cell.

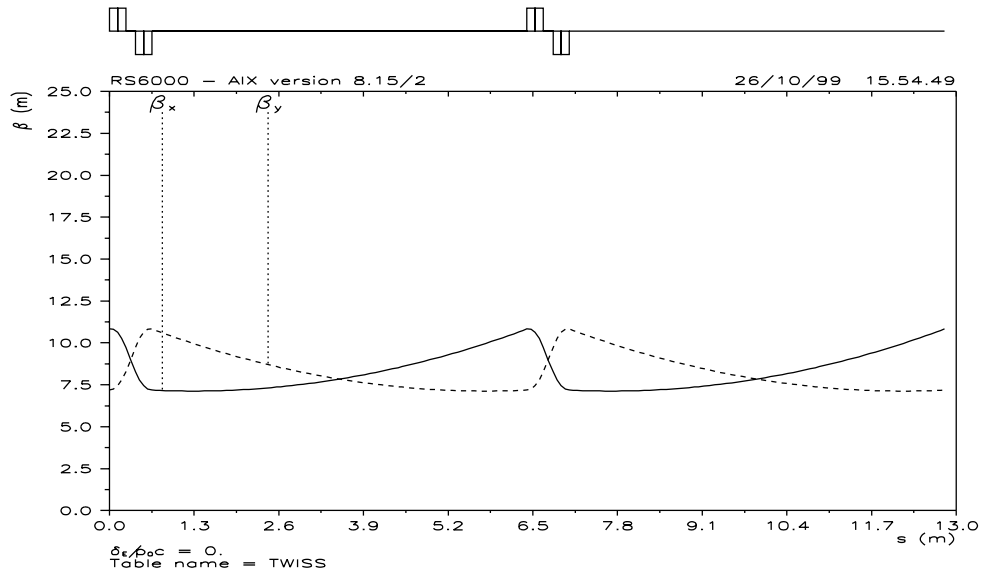


Figure 5:  $\beta$ -functions in the  $90^\circ$  FDOFDO cell with 3 rf-structures per half-cell.

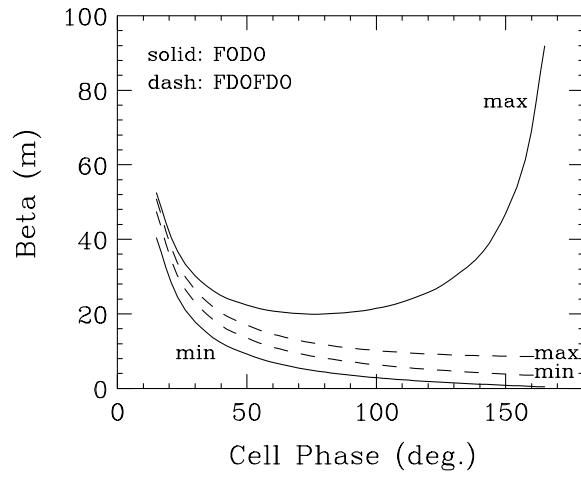


Figure 6: Maximum and minimum  $\beta$ -functions in the FODO (solid) and FDOFDO (dash) cells as a function of cell phase advance.

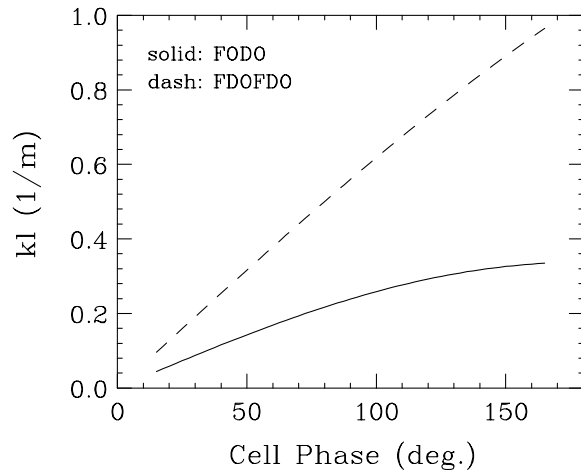


Figure 7: Single quadrupole strength  $kl$  in the FODO (solid) and FDOFDO (dash) cells as a function of cell phase advance.

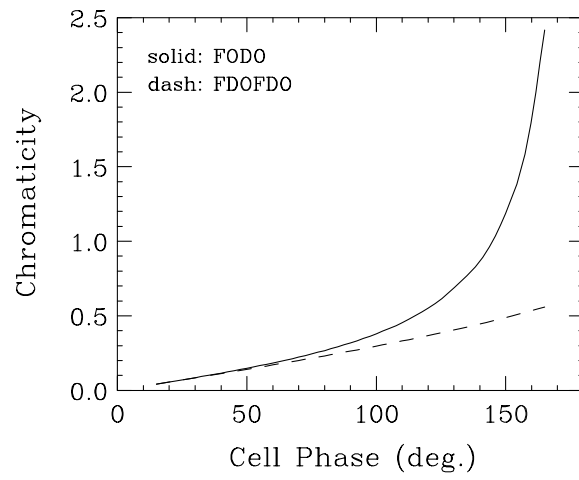


Figure 8: Linear chromaticity per FODO (solid) and FDOFDO (dash) cell as a function of cell phase advance.

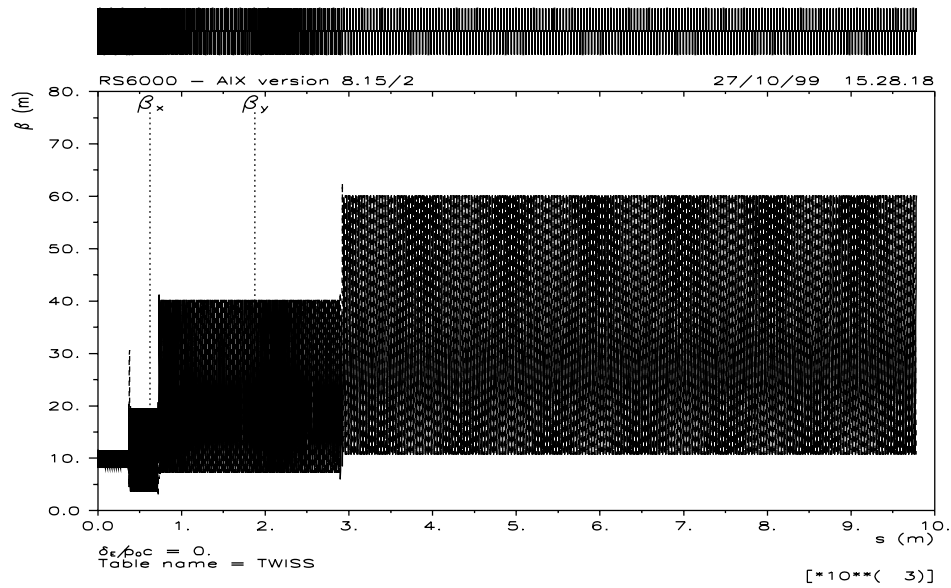


Figure 9:  $\beta$ -functions in the FODO-3D6 lattice based on 3 rf-structures per girder.

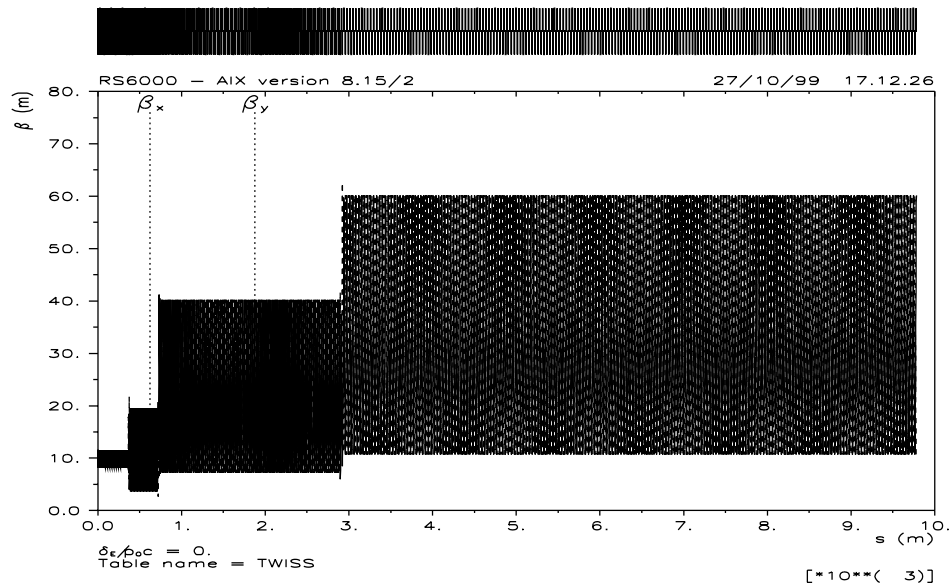


Figure 10:  $\beta$ -functions in the FODO-3D8 lattice based on 3 rf-structures per girder.

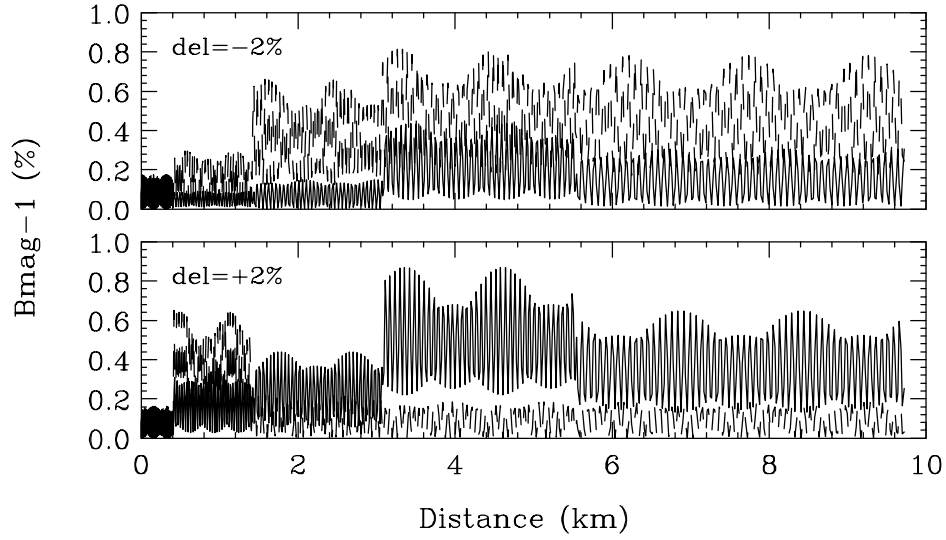


Figure 11:  $B_{mag}-1$  function in the FODO-2 lattice at  $\delta = \pm 2\%$  (solid -  $x$ , dash -  $y$ ).

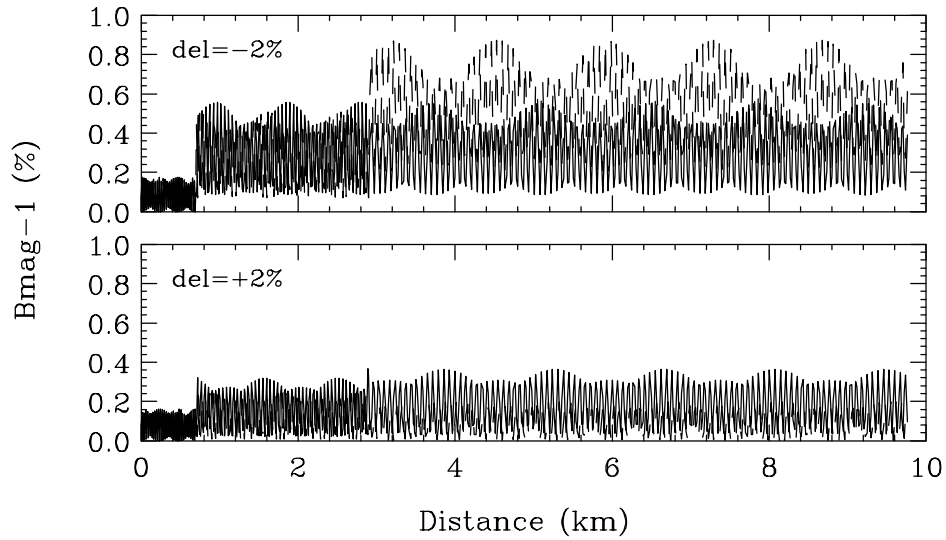


Figure 12:  $B_{mag}-1$  function in the FODO-3 lattice at  $\delta = \pm 2\%$  (solid -  $x$ , dash -  $y$ ).

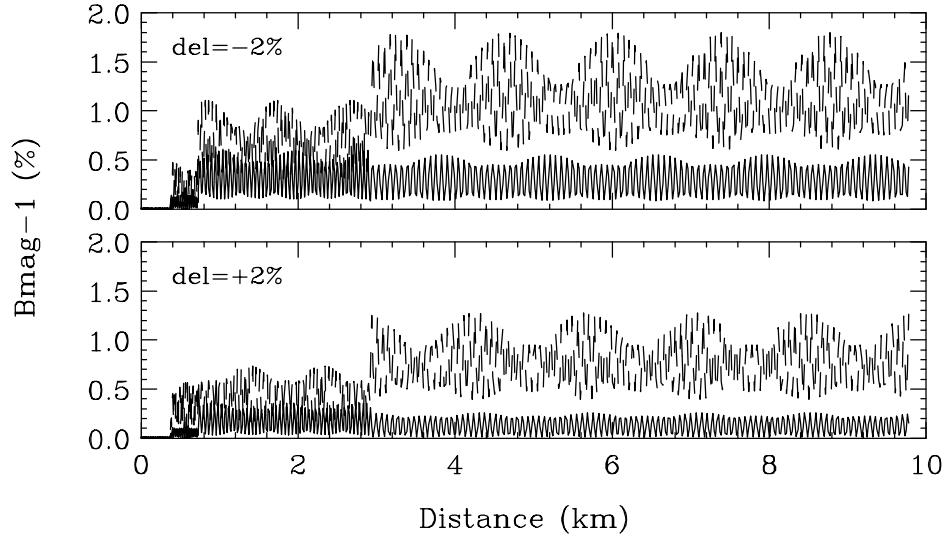


Figure 13:  $B_{mag}-1$  function in the FODO-3D6 lattice at  $\delta = \pm 2\%$  (solid -  $x$ , dash -  $y$ ).

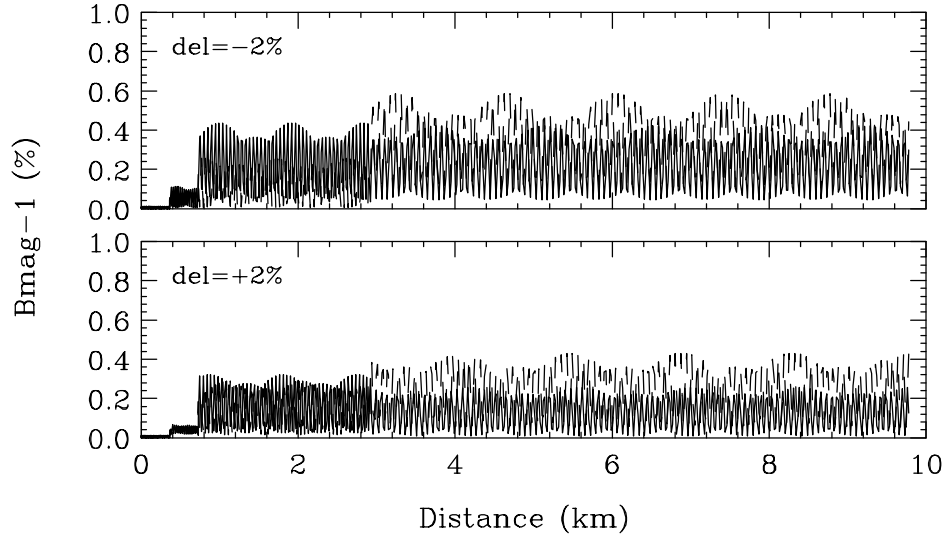


Figure 14:  $B_{mag}-1$  function in the FODO-3D8 lattice at  $\delta = \pm 2\%$  (solid -  $x$ , dash -  $y$ ).

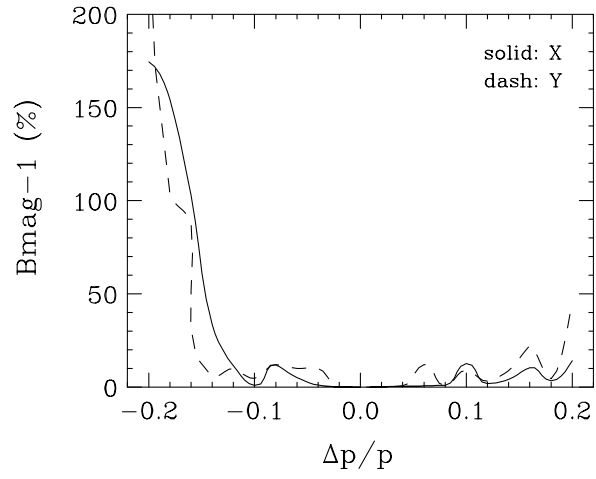


Figure 15:  $B_{mag} - 1$  function versus  $\delta$  at the end of the FODO-2 lattice.

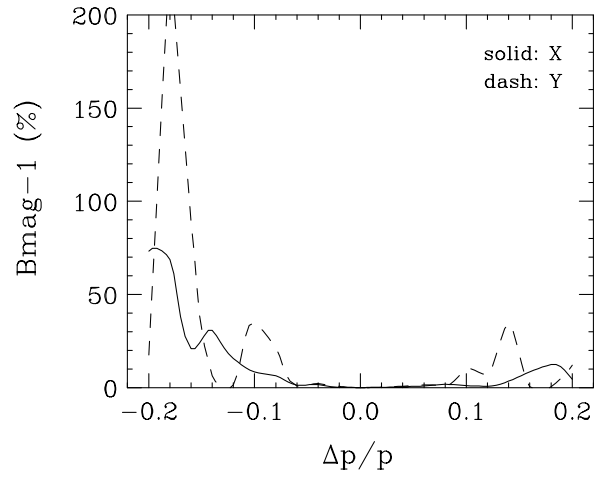


Figure 16:  $B_{mag} - 1$  function versus  $\delta$  at the end of the FODO-3 lattice.

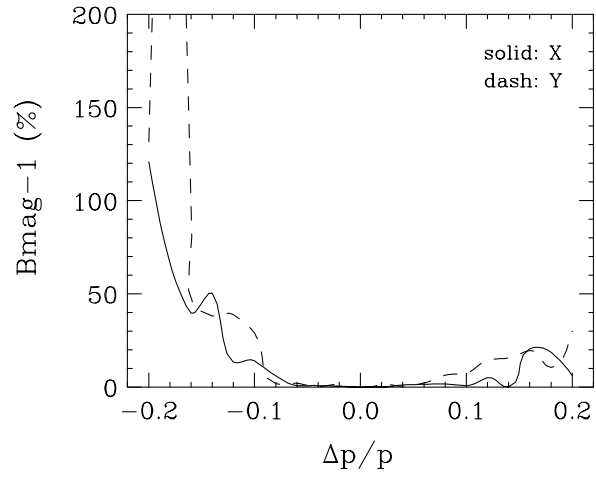


Figure 17:  $B_{mag}-1$  function versus  $\delta$  at the end of the FODO-3D6 lattice.

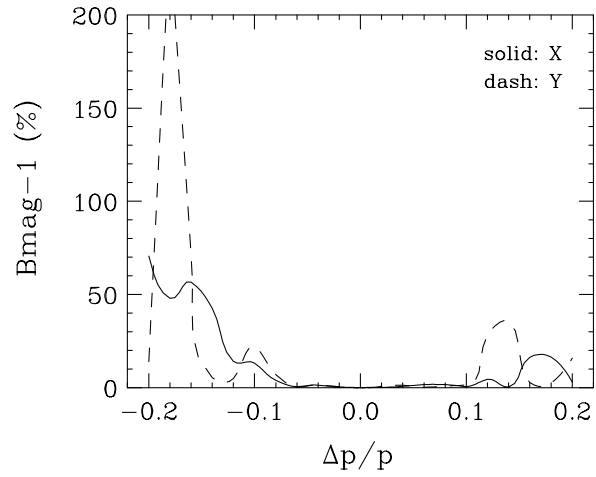


Figure 18:  $B_{mag}-1$  function versus  $\delta$  at the end of the FODO-3D8 lattice.

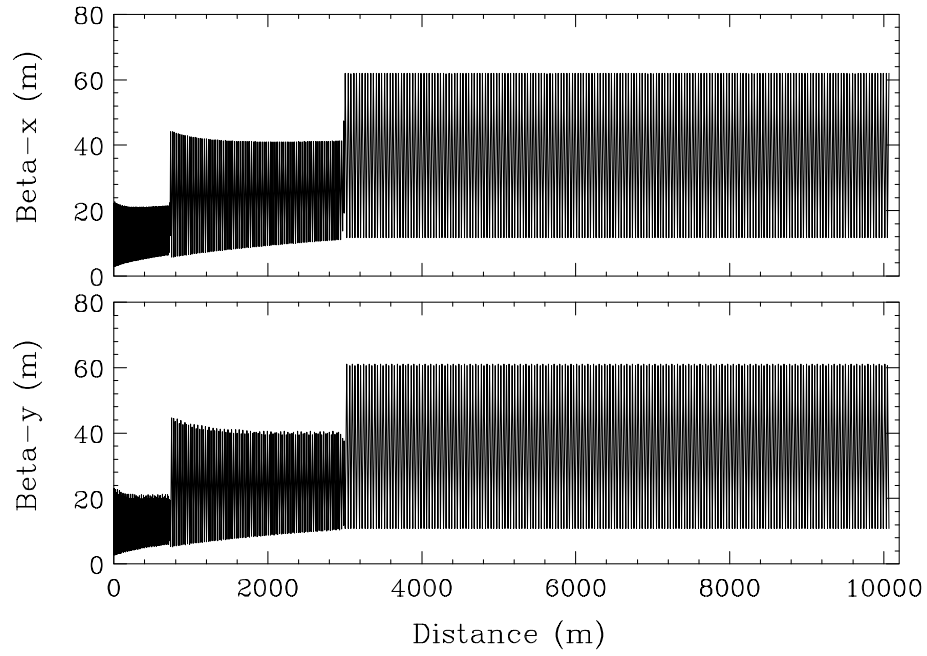


Figure 19:  $\beta$ -functions in the FODO-100 lattice.

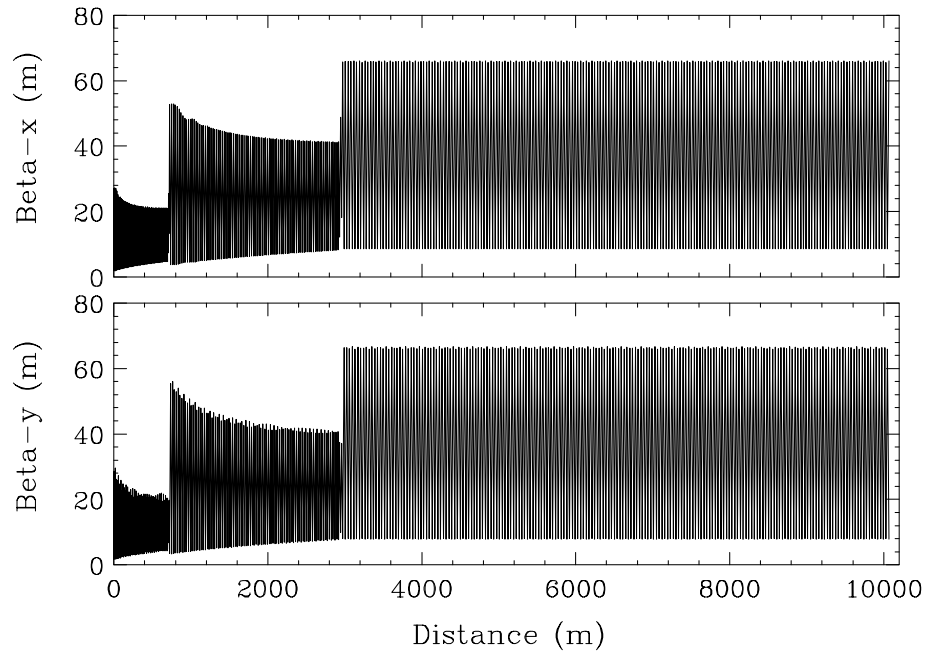


Figure 20:  $\beta$ -functions in the FODO-120 lattice.

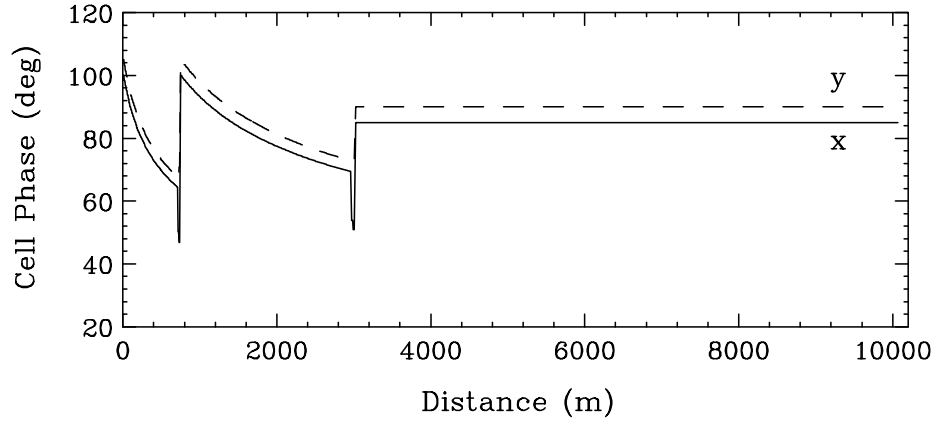


Figure 21: Phase advance per cell in the FODO-100 lattice.

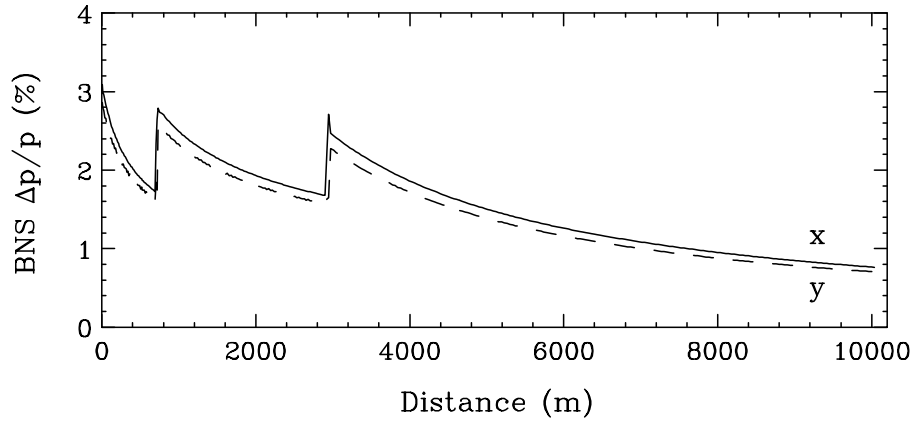


Figure 22: Desired BNS autophasing energy spread in the FODO-100 lattice.

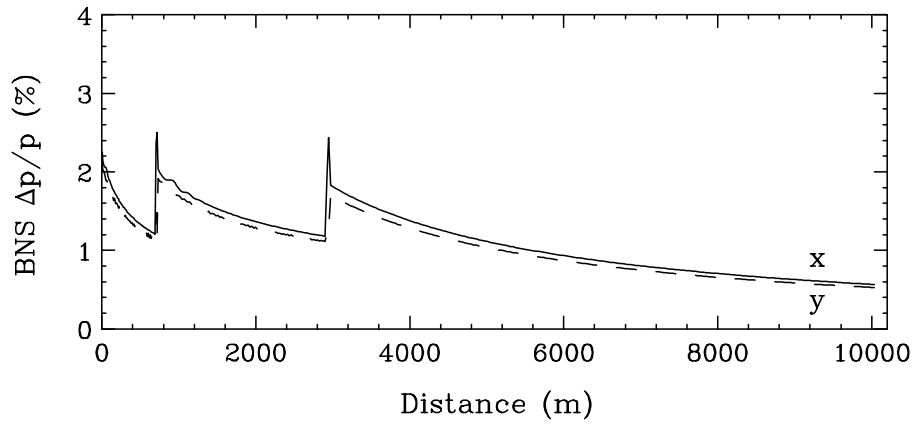


Figure 23: Desired BNS autophasing energy spread in the FODO-120 lattice.

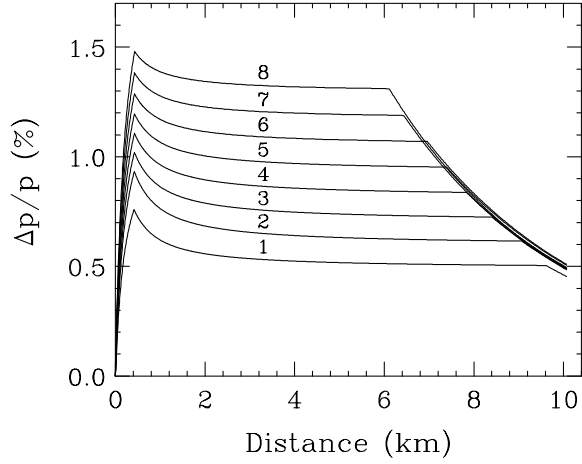


Figure 24: Beam rms energy spread along the linac for 8 rf-phase configurations in the FODO-100, FODO-120 and FODO-140 options.

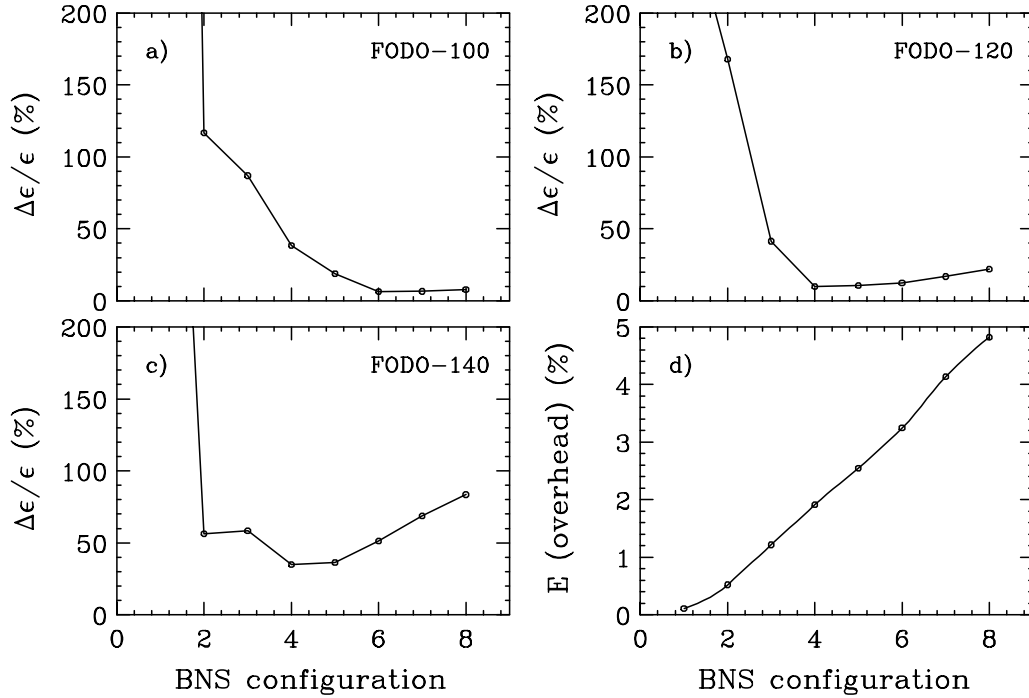


Figure 25: Vertical emittance growth with  $1\sigma_y$  initial beam offset for the FODO-100, FODO-120 and FODO-140 options (a, b, c); and energy overhead (d) as a function of BNS configuration.

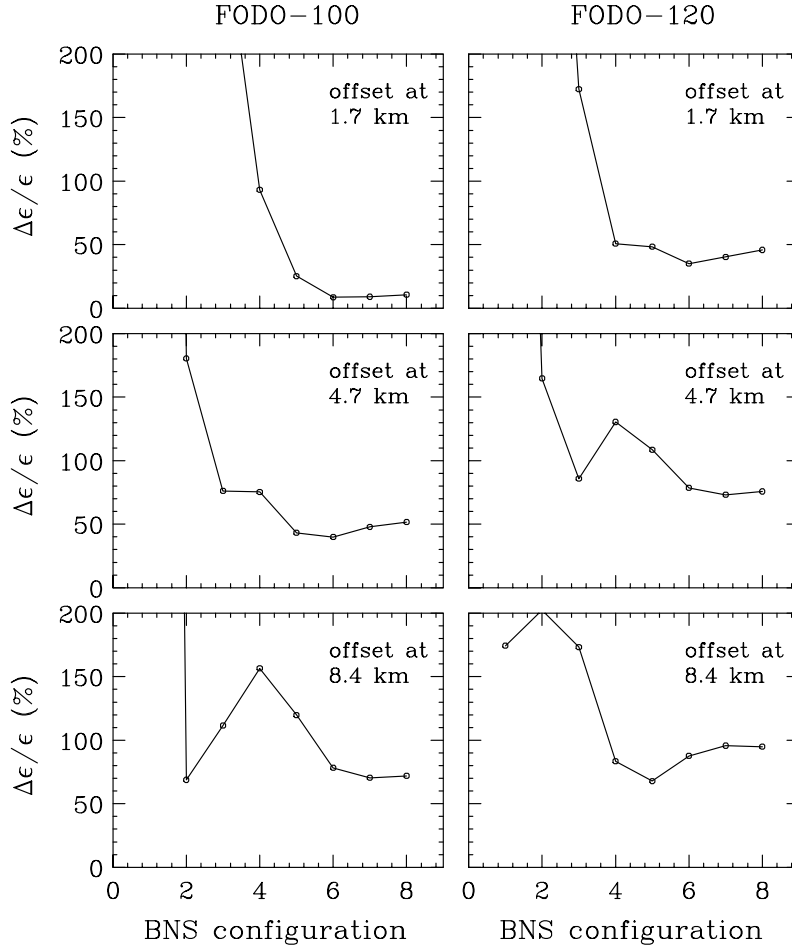


Figure 26: Vertical emittance growth with  $1\sigma_y$  initial beam offset and  $y = 0.5 \mu\text{m}$  single D-quad offset for the FODO-100 and FODO-120 options as a function of BNS configuration.

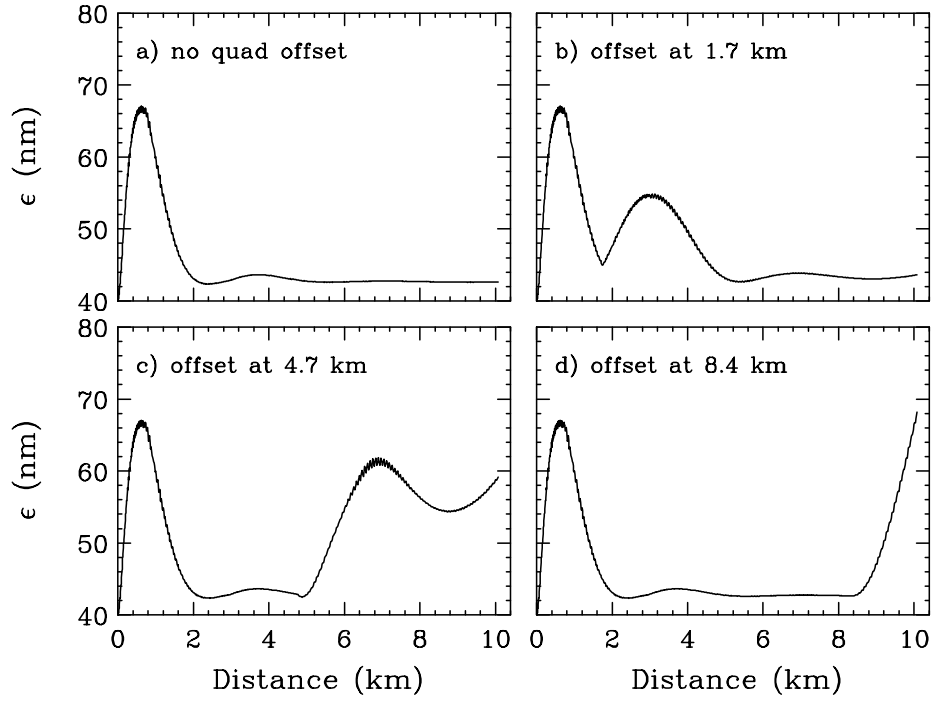


Figure 27: Vertical emittance with  $1\sigma_y$  initial beam offset and  $y = 0.5 \mu\text{m}$  single D-quad offset for the FODO-100 lattice and BNS configuration 7.

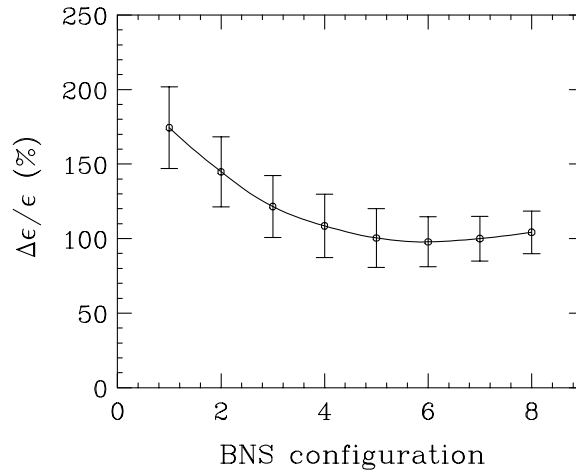


Figure 28: Vertical emittance growth with  $1\sigma_y$  initial beam offset and  $y_{rms} = 10 \mu\text{m}$  structure misalignment for the FODO-100 lattice as a function of BNS configuration.